Ab initio quantum approach to planar helium under periodic driving

Javier Madroñero
Physik Department, Technische Universität München, 85747 Garching, Germany
and PAMO, Université Catholique de Louvain, 2, Chemin du Cyclotron, 1348 Louvain-la-Neuve, Belgium

Andreas Buchleitner
Physikalisches Institut, Albert-Ludwigs-Universität Freiburg, Hermann-Herder-Str. 3, D-79104 Freiburg
and Max-Planck-Institut für Physik Komplexer Systeme, Dresden, Germany
(Received 13 February 2008; published 12 May 2008)

We present a method for the accurate quantum treatment of the planar three-body Coulomb problem under electromagnetic driving. Our *ab initio* approach combines Floquet theory, complex dilation, and the representation of the Hamiltonian in suitably chosen coordinates, without adjustable parameters. The resulting complex-symmetric sparse banded generalized eigenvalue problem of rather high dimension is solved using advanced techniques of parallel programming. This theoretical and numerical machinery is employed to provide a complete description of the bound and of the doubly excited spectrum of the field-free two-dimensional (2D) helium atom. For the driven atom, we focus on the near resonantly driven frozen planet configuration, and give evidence for the existence of nondispersive two-electron wave packets.

DOI: 10.1103/PhysRevA.77.053402 PACS number(s): 32.30.−r, 31.15.vj, 32.80.Qk

I. INTRODUCTION

After hydrogen, helium is the simplest naturally available atomic species. But at the same time, helium is one of the simplest systems where neither the classical nor the quantum dynamics are integrable. Indeed, for this microscopic realization of the three-body problem of celestial mechanics (with gravitational forces replaced by attractive and repulsive Coulomb interactions), the two-electron dynamics is in general irregular or chaotic, with only rather small domains of classical phase space occupied by regular, i.e., integrable motion. This loss of integrability, due to the electron-electron interaction, caused the failure of first quantization attempts on the basis of Bohr's quantum postulates [1]. Only with the development of the modern semiclassical theory [2,3] and the subsequent semiclassical quantization of helium [4,5] was the nonintegrability of the quantum system understood as the direct counterpart of the corresponding classical mixed regular-chaotic dynamics [6].

Under the action of an additional electromagnetic field, the complexity of both, the classical and the quantum dynamics, increases dramatically. As compared to one-electron atoms, helium adds the additional electron-electron interaction term, which also is a source of electronic correlations. Manifestations of interelectronic repulsion in driven helium have been observed in the double ionization of helium from the ground state, by strong laser fields [7,8]: Strong enhancement (by several orders of magnitude) of the doubly charged ion production as compared to the yield expected on the basis of a single active electron approximation [9,10]—where the electron-electron interaction is neglected—was observed, and interpreted as a fingerprint of correlated electronic ionization processes (manifesting in *nonsequential* ionization as opposed to *sequential* ionization, in the independent electrons picture), where one electron is "knocked out" by the other during a laser-induced recollision process. On the theoretical side, a number of rather restrictive nonsequential models [7,11,12] can fit many coarse-grained features of the experiment. However, none of these models can fully describe the geometry of the fragmentation process observed in more refined experiments [13,14]—which also reveal a clear dependence of the excitation and ionization process on the electronic structure [15] of He-like atoms.

While electronic correlations are essentially brought about by the kinematics of the double ionization process sketched above, it is also feasible to prepare the atom in a highly correlated initial state: Strong electronic correlations are found in doubly excited states of unperturbed helium. These highly asymmetric, though very stable states are well localized along the frozen planet configuration [6,16,17], characterized by highly correlated classical dynamics of the electrons. Under near-resonant periodic driving these states transform into nondispersive wave packets [18,19], in one-dimensional (1D) quantum calculations [20,21]. However, until now, no evidence of the existence of these objects has been found in realistic quantum calculations in more than one dimension. This is a crucial issue, given the potential of nondispersive wave packets for coherent control and quantum information [22], on the one hand, and the nontrivial role of the dimension of the accessible configuration space suggested by classical calculations and quantum spectra of the unperturbed atom, on the other [23–25]. So far, only results of diffusion Monte Carlo calculations suggest the existence of nondispersive two-electron wave packets along Langmuir orbits, under the *combined* action of circularly polarized electromagnetic and static magnetic fields [25].

A clear understanding of all the above issues requires an accurate theoretical treatment of driven helium. The latter defines a formidable theoretical and numerical challenge: Even in the simplest case of the field-free, 3D helium atom currently available approaches can only access a regime of rather low doubly excited states and low angular momentum. This is due to the rapid increase of the required basis size, and of the number of nonzero matrix elements of the Hamiltonian as the excitation or the angular momentum is increased [26–29]. An additional, linearly polarized electro-

magnetic field will mix almost all good quantum numbers of the field-free case, and only the projection of the total angular momentum onto the polarization axis of the field, and a generalized parity which encompasses the phase of the driving field, remain conserved. Consequently, the density of states dramatically increases with the excitation of the electrons, as well as with the order of the multiphoton excitation process induced by the external field. Therefore, a fully three-dimensional treatment of the driven helium problem for arbitrary driving frequencies and electronic excitations still remains beyond reach even of the largest supercomputers currently available, simply due to the rapidly increasing size of Hilbert space as more and more angular momenta are coupled. Note, however, that three-dimensional *ab initio* treatments [29–33] of the ionization of helium from the atomic ground state are available, though cannot resolve the transient population of highly excited states in the course of the ionization process. Neither has it been demonstrated so far that these approaches bear the potential to describe the dynamics of highly excited initial states under electromagnetic driving.

Here we present an approach to the driven three-body Coulomb problem, confined to a planar configuration space, with the field polarization axis in the plane. While such confinement certainly restricts the generality of our model, semiclassical scaling arguments suggest that the unperturbed three-body dynamics is essentially planar at high electronic excitations and small to moderate total angular momenta [34]. Equally so, highly correlated fragmentation processes starting from the atomic ground state appear to be mediated by essentially two-dimensional configurations [15,35]. Beyond the atomic problem to which we will apply our machinery in this contribution, the planar three-body Coulomb problem also has realizations in quasi-two-dimensional semiconductor structures [36–41], as well as in 2D quantum dots [42]. As we will see, our approach to the problem allows a description of driven helium in the entire parameter range of weakly and doubly excited states, under optical as well as microwave fields.

The paper is organized as follows: in Sec. II we outline our theoretical setup, valid equally well for the exact quantum description of field-free and of driven planar helium, without adjustable parameters, designed for direct access to the detailed spectral structure of the problem. Section III describes the numerical implementation of our setup. Section IV provides a complete description of the spectral properties of field-free planar helium. Section V presents Rydberg series of doubly excited states of 2D helium localized along frozen planet trajectories, and discusses their stability properties when the atom is subject to an external driving. Section VI concludes the paper.

II. THEORY

The problem we have to describe with a minimum of approximations is a helium atom exposed to a periodic monochromatic driving field. The electrons are subject to the combined potentials of the nucleus and of the interelectronic repulsion, and are driven and eventually ionized by the external field. Therefore, our theoretical approach has to account for the following:

(i) The singularities of the Coulomb potentials.

(ii) The spectrum of the field-free atom consisting of bound states, and of resonances embedded into the atomic cotinua.

(iii) The spectrum of the atom "dressed" by the field.

To do so, we have to combine various tools.

A. Hamiltonian

In dipole approximation, employing the length gauge and neglecting relativistic and QED terms, the Hamiltonian of a helium atom exposed to a linearly polarized electromagnetic field, of frequency $\omega=2\pi/T$ and amplitude F, reads, in atomic units,

$$H = H_0 + F(x_1 + x_2)\cos(\omega t), \tag{1}$$

where

$$H_0 = \frac{\boldsymbol{p}_1^2 + \boldsymbol{p}_2^2}{2} - \frac{Z}{r_1} - \frac{Z}{r_2} + \frac{\gamma}{r_{12}}, \tag{2}$$

with $Z=2$ and $\gamma=1$, is the Hamiltonian of the field-free atom with fixed nucleus. Here, r_1 and r_2 are the distances of the electrons from the nucleus, and r_{12} is the interelectronic separation.

Both the classical and the quantum dynamics are governed by the Hamiltonian (1) and (2). The classical dynamics generated by the Hamiltonian (2) is invariant under the scaling transformations [43]

$$H_0 \mapsto |E|^{-1} H_0,$$

$$\boldsymbol{r}_i \mapsto |E| \boldsymbol{r}_i, \quad i = 1,2,$$

$$\boldsymbol{p}_i \mapsto |E|^{-1/2} \boldsymbol{p}_i, \quad i = 1,2,$$

$$t \mapsto |E|^{3/2} t, \tag{3}$$

where E is the energy of the two-electron system. This scale invariance also holds for driven helium, where, additionally, the scaled field amplitude and the scaled frequency are obtained by the transformations

$$F \mapsto |E|^{-2} F,$$

$$\omega \mapsto |E|^{-3/2} \omega. \tag{4}$$

From (3), the angular momentum scales as $L^{sc}=|E|^{1/2}L$. Therefore, for moderate values of L and highly doubly excited states ($E \simeq 0$), the scaled angular momentum is close to zero, tantamount to an almost planar three-body configuration. Precisely this is the semiclassical energy regime where one expects that classical and quantum dynamics are similar.

From now on, we confine the dynamics to two dimensions of configuration space, with the Cartesian positions (x_1, y_1) and (x_2, y_2) of the electrons. The planar helium dynamics thus has four degrees of freedom which span an eight-dimensional phase space.

B. Folquet theory

The Hamiltonian (1) is periodic in time, with period $T=2\pi/\omega$. For such systems, the Floquet theorem [44] guarantees that the solutions $|\psi(t)\rangle=|\psi(\boldsymbol{r}_1,\boldsymbol{r}_2,t)\rangle$ of the Schrödinger equation associated with (1) can be expressed as superpositions of time periodic wave functions $|\phi_{\varepsilon_i}(t)\rangle=|\phi_{\varepsilon_i}(\boldsymbol{r}_1,\boldsymbol{r}_2,t)\rangle$ [45],

$$|\psi(t)\rangle = \sum_i c_i \exp(-i\varepsilon_i t)|\phi_{\varepsilon_i}(t)\rangle, \tag{5}$$

with $|\phi_{\varepsilon_i}(t+T)\rangle=|\phi_{\varepsilon_i}(t)\rangle$ and constant coefficients c_i. The ε_i and $|\phi_{\varepsilon_i}(t)\rangle$ are called *quasienergies* and *Floquet states*, respectively, and are given as the eigenvalues and eigenvectors of the Floquet operator [45,46]

$$\mathcal{H}_F = H(t) - i\frac{\partial}{\partial t} \tag{6}$$

acting on the extended (by time, considered now as a generalized coordinate [47]) Hilbert space of square integrable, time periodic functions, $\mathcal{L}^2(\mathbb{R}^4)\otimes\mathcal{L}^2(\mathbb{T}_\omega)$ [96] i.e.,

$$\mathcal{H}_F|\phi_{\varepsilon_i}(t)\rangle = \varepsilon_i|\phi_{\varepsilon_i}(t)\rangle. \tag{7}$$

Introducing the Fourier components of the Floquet states

$$|\phi_{\varepsilon_i}(t)\rangle = \sum_{k=-\infty}^{\infty} e^{-ik\omega t}|\phi_{\varepsilon_i}^k\rangle, \tag{8}$$

the time-dependent problem (7) can be rewritten as a coupled set of time-independent equations

$$(\varepsilon_i - H_0 + k\omega)|\phi_{\varepsilon_i}^k\rangle = \frac{F}{2}(x_1+x_2)(|\phi_{\varepsilon_i}^{k+1}\rangle + |\phi_{\varepsilon_i}^{k-1}\rangle), \tag{9}$$

where the additional quantum number counts the number of photons $k\in\mathbb{Z}$ exchanged between the atom and the field [45]. Notice that for the field-free case ($F=0$ and $\omega=0$) Eq. (9) reduces to the standard eigenvalue problem on $\mathcal{L}^2(\mathbb{R}^4)$.

C. Complex dilation

The electron-electron interaction in helium couples different channels of the noninteracting two-electron dynamics, and gives rise to resonance states embedded in the continua above the first single electron ionization threshold. In the presence of an electromagnetic field, since k is running from $-\infty$ to $+\infty$ in Eq. (9), the dipole term in Eq. (1) couples *all* remaining bound states of the field-free atom to the continuum. Therefore, the spectrum of Eq. (7) exclusively consists of resonance states, with quasienergies ε_i and finite lifetimes $1/\Gamma_i$, embedded in the continuum. Poles or autoionizing states of the field-free atom are coupled by the driving field, what results in a strong modification of the pole structure of the system in the complex plane, and strongly enhances the effective density of states, due to the periodicity of the Floquet spectrum. To extract the resonance states and their decay rates we use complex rotation (or "dilation") [48–50], which was shown to be applicable for the Coulomb potential and in the Floquet picture in [51] and [52], respectively.

The complex dialation of any operator by an angle θ is mediated by the nonunitary complex rotation operator

$$R(\theta) = \exp\left(-\theta\frac{\boldsymbol{r}\cdot\boldsymbol{p}+\boldsymbol{p}\cdot\boldsymbol{r}}{2}\right). \tag{10}$$

Rotation of the position and momentum operators in the complex plane according to

$$\boldsymbol{r} \to R(\theta)\boldsymbol{r}R(-\theta) = \boldsymbol{r}e^{i\theta},$$

$$\boldsymbol{p} \to R(\theta)\boldsymbol{p}R(-\theta) = \boldsymbol{p}e^{-i\theta}, \tag{11}$$

transforms the unperturbed Hamiltonian (2) and the Floquet Hamiltonian (6) in complex symmetric operators with complex eigenvalues. However, the spectrum of the rotated Hamiltonian has the following important properties [49,51–53]:

(a) The bound spectrum of H_0 is invariant under the complex rotation.

(b) The spectrum of the rotated Floquet Hamiltonian is periodic with period ω, as for the original Hamiltonian.

(c) The continuum states are located on half lines, rotated by an angle -2θ around the ionization thresholds of the unrotated Hamiltonian, into the lower half of the complex plane. In the specific case of the unperturbed 2D helium Hamiltonian (2), in analogy to the 3D case [53], the continuum states are rotated around the single ionization thresholds $I_N=-Z^2/[2(N-1/2)^2]$ [54], with $N=1,2,3,\ldots$. In the case of the Floquet operator, they are rotated around the multiphoton ionization thresholds $I_N+k\omega$ (k integer).

(d) There are isolated complex eigenvalues $\varepsilon_i=E_i-i\Gamma_i/2$ in the lower half plane, corresponding to resonance states. These are stationary under changes of θ, provided the dilation angle is large enough to uncover their positions on the Riemannian sheets of the associated resolvent [53,55]. The associated resonance eigenfunctions are square integrable [50], in contrast to the resonance eigenfunctions of the unrotated Hamiltonian. The latter are asymptotically diverging outgoing waves [50,56].

D. Appropriate coordinates

All relevant physical information is contained in the spectrum of the rotated Hamiltonian, and can be obtained by a subsequent diagonalization. However, one of the main difficulties to actually perform this diagonalization are the Coulomb singularities in the Hamiltonian (2). Nevertheless, choosing an appropriate representation in parabolic coordinates [54], the singularities are rigorously regularized. The appropriate set of parabolic coordinates is obtained after three subsequent coordinate transformations. We start with the Cartesian coordinates of both electrons, (x_1,y_1) and (x_2,y_2), respectively. After the first transformation, only r_1 and r_2 are polynomial functions of the new coordinates μ_i, ν_i, $i=1,2$:

$$x_i = \frac{1}{2}(\mu_i^2 - \nu_i^2), \quad \mu_i = \sqrt{r_i + x_i},$$

$$y_i = \mu_i\nu_i, \quad \nu_i = \sqrt{r_i - x_i},$$

$$r_i = \sqrt{x_i^2 + y_i^2} = \frac{1}{2}(\mu_i^2 + \nu_i^2), \quad i = 1,2, \tag{12}$$

while r_{12} still involves square root functions of μ_i, ν_i.

The second transformation consists just in a rotation by 45° of each pair (μ_1, μ_2) and (ν_1, ν_2) of the new coordinates:

$$\mu_p = (\mu_1 + \mu_2)/\sqrt{2}, \quad \mu_1 = (\mu_p + \mu_m)/\sqrt{2},$$

$$\mu_m = (\mu_1 - \mu_2)/\sqrt{2}, \quad \mu_2 = (\mu_p - \mu_m)/\sqrt{2},$$

$$\nu_p = (\nu_1 + \nu_2)/\sqrt{2}, \quad \nu_1 = (\nu_p + \nu_m)/\sqrt{2},$$

$$\nu_m = (\nu_1 - \nu_2)/\sqrt{2}, \quad \nu_2 = (\nu_p - \nu_m)/\sqrt{2}. \tag{13}$$

Hereafter, we have $r_{12} = \sqrt{(\mu_p^2 + \nu_p^2)(\mu_m^2 + \nu_m^2)}$. Hence, after another parabolic transformation, also r_{12} will be a polynomial function of the coordinates. Our final coordinate set is thus defined as

$$\mu_p = (x_p^2 - y_p^2)/2, \quad x_p = \sqrt{r_p + \mu_p},$$

$$\nu_p = x_p y_p, \quad y_p = \sqrt{r_p - \mu_p},$$

$$\mu_m = (x_m^2 - y_m^2)/2, \quad x_m = \sqrt{r_m + \mu_m},$$

$$\nu_m = x_m y_m, \quad y_m = \sqrt{r_m - \mu_m},$$

$$r_p = \sqrt{\mu_p^2 + \nu_p^2} = x_p^2 + y_p^2,$$

$$r_m = \sqrt{\mu_m^2 + \nu_m^2} = x_m^2 + y_m^2, \tag{14}$$

leading to the following representation of r_1, r_2, and r_{12} in terms of x_p, y_p, x_m, and y_m:

$$16 r_1 = [(x_p - y_m)^2 + (x_m + y_p)^2] \times [(x_p + y_m)^2 + (x_m - y_p)^2],$$

$$16 r_2 = [(x_p - x_m)^2 + (y_p - y_m)^2] \times [(x_p + x_m)^2 + (y_p + y_m)^2],$$

$$4 r_{12} = (x_p^2 + y_p^2)(x_m^2 + y_m^2). \tag{15}$$

The Jacobian of the complete transformation reads

$$B = J_1 J_2 J_3 = 16 r_1 r_2 r_{12}. \tag{16}$$

In parabolic coordinates, the eigenvalue problem (9) is regularized by multiplication with the Jacobian (16). Thus, the regularized, rotated Floquet eigenvalue problem takes the form

$$(\varepsilon_i B + e^{-2i\theta} T - e^{-i\theta} V + k\omega B)|\phi_{\varepsilon_i}^k\rangle = \mathcal{F}(\theta)(|\phi_{\varepsilon_i}^{k+1}\rangle + |\phi_{\varepsilon_i}^{k-1}\rangle), \tag{17}$$

where T, V, and $\mathcal{F}(\theta)$ are given by

$$T = 16 r_1 r_2 r_{12}(\nabla_1^2 + \nabla_2^2), \tag{18}$$

$$V = -16 Z r_2 r_{12} - 16 Z r_1 r_{12} + 16\gamma r_1 r_2, \tag{19}$$

$$\mathcal{F}(\theta) = \frac{1}{2} F e^{i\theta}(x_1 + x_2) B. \tag{20}$$

The explicit expression for the potential term V in terms of parabolic coordinates follows upon substitution of Eq. (15). The expression for the kinetic term T and for the field term $\mathcal{F}(\theta)$ are a bit more complicated,

$$\begin{aligned} T = (r_1 + r_2)&\left\{ (x_p^2 + y_p^2)\left(\frac{\partial^2}{\partial x_m^2} + \frac{\partial^2}{\partial y_m^2} \right) \right. \\ &\left. + (x_m^2 + y_m^2)\left(\frac{\partial^2}{\partial x_p^2} + \frac{\partial^2}{\partial y_p^2} \right) \right\} \\ &+ 2(r_2 - r_1)\left\{ (x_m x_p + y_m y_p)\left(\frac{\partial^2}{\partial x_m \partial x_p} + \frac{\partial^2}{\partial y_m \partial y_p} \right) \right. \\ &\left. + (y_m x_p - x_m y_p)\left(\frac{\partial^2}{\partial x_m \partial y_p} - \frac{\partial^2}{\partial y_m \partial x_p} \right) \right\} \end{aligned} \tag{21}$$

and

$$\mathcal{F}(\theta) = \frac{1}{16} F e^{i\theta}(x_p^4 + y_p^4 + x_m^4 + y_m^4 - 6x_m^2 y_m^2 - 6x_p^2 y_p^2) B. \tag{22}$$

T and V are polynomial functions of 8th degree in the parabolic coordinates x_p, y_p, x_m, y_m, and in their partial derivatives ∂_{x_p}, ∂_{y_p}, ∂_{x_m}, ∂_{y_m}. The Jacobian B and the field term $\mathcal{F}(\theta)$ have polynomial expressions of degree 12 and 16, respectively. Therefore, the various terms of the generalized eigenvalue problem (17) are polynomials in the coordinates and conjugate momenta, and can be expressed using the corresponding creation and annihilation operators. For instance,

$$a_{x_p} = \frac{1}{\sqrt{2}}(x_p + i p_{x_p}), \quad a_{x_p}^\dagger = \frac{1}{\sqrt{2}}(x_p - i p_{x_p}). \tag{23}$$

$a_{x_m}, a_{x_m}^\dagger, a_{y_p}, a_{y_p}^\dagger, a_{y_m}$, and $a_{y_m}^\dagger$ are analogously defined. From these expressions we introduce the right and left circular operators in the planes (x_p, y_p) and (x_m, y_m), defined by

$$a_1 = (a_{x_p} - i a_{y_p})/\sqrt{2},$$

$$a_2 = (a_{x_p} + i a_{y_p})/\sqrt{2},$$

$$a_3 = (a_{x_m} - i a_{y_m})/\sqrt{2},$$

$$a_4 = (a_{x_m} + i a_{y_m})/\sqrt{2}. \tag{24}$$

The first few terms of the expression for $\mathcal{F}(\theta)$ read

$$\mathcal{F}(\theta) = \frac{1}{2} e^{i\theta}\left(\frac{945 a_1^4}{64} + \frac{945}{64} a_1^5 a_2 + \frac{a_1^9 a_2^5}{1024} + \cdots \right). \tag{25}$$

The full expression for this operator in normal order (creation operators on the left [57]) has 5472 terms [58]. Together with the expressions for the other operators involved in Eq. (22), these were obtained using a home-made MATHEMATICA code. The polynomial expressions for T, V, and B have 335, 357, and 1463 terms, respectively. A much simpler

expression is available for the angular momentum L_z:

$$L_z = \frac{1}{4}(a_1^\dagger a_1 - a_2^\dagger a_2 + a_3^\dagger a_3 - a_4^\dagger a_4) = \frac{1}{4}(N_1 - N_2 + N_3 - N_4), \tag{26}$$

where $N_i = a_i^\dagger a_i$ are the corresponding number operators.

E. Selection rules

Since the circular operators satisfy the usual commutation relations,

$$[a_i, a_j] = 0, \quad [a_i^\dagger, a_j^\dagger] = 0, \quad [a_i, a_j^\dagger] = \delta_{ij}, \tag{27}$$

for $i,j=1,2,3,4$, we can associate a harmonic oscillator with each pair of circular operators $a_i^\dagger$ and a_i, what induces a natural basis set composed of tensor products of harmonic oscillator Fock states:

$$|n_1 n_2 n_3 n_4\rangle = |n_1\rangle \otimes |n_2\rangle \otimes |n_3\rangle \otimes |n_4\rangle. \tag{28}$$

Due to the strictly polynomial form of Eq. (17) in the circular operators, each basis state couples to a limited number of states. Whether two states are coupled or not by some operator A is determined by a *selection rule* defined in the following way: Two elements $|n_1 n_2 n_3 n_4\rangle$ and $|n_1' n_2' n_3' n_4'\rangle$ of the basis set (28) are coupled or satisfy the selection rule $\{\Delta n_1, \Delta n_2, \Delta n_3, \Delta n_4\}$, with $\Delta n_i = n_i - n_i'$, if $\langle n_1 n_2 n_3 n_4 | A | n_1' n_2' n_3' n_4' \rangle \neq 0$. It is found that $\mathcal{F}(\theta)$ has 488 selection rules, while the Jacobian B has 155 and the sum of the kinetic and potential operators $-1/2T+V$ has 91 [58]. For a given selection rule $\Delta \boldsymbol{n} = \{\Delta n_1, \Delta n_2, \Delta n_3, \Delta n_4\}$, the matrix elements $\langle \boldsymbol{n} + \Delta \boldsymbol{n} | -1/2T + V | \boldsymbol{n} \rangle$ and $\langle \boldsymbol{n} + \Delta \boldsymbol{n} | B | \boldsymbol{n} \rangle$, with $|\boldsymbol{n}\rangle = |n_1 n_2 n_3 n_4\rangle$ and $|\boldsymbol{n} + \Delta \boldsymbol{n}\rangle = |n_1 + \Delta n_1 n_2 + \Delta n_2 n_3 + \Delta n_3 n_4 + \Delta n_4\rangle$, involve square roots of integer numbers and depend only on n_1, n_2, n_3, and n_4. For example, the matrix element of the operator $\mathcal{F}(\theta)$ for the selection rule $\Delta \boldsymbol{n} = \{-9, -5, 0, 0\}$ reads

$$\begin{aligned} &\langle \boldsymbol{n} + \Delta \boldsymbol{n} | \mathcal{F}(\theta) | \boldsymbol{n} \rangle \\ &\quad = \sqrt{n_1(n_1-1)\cdots(n_1-8)}\sqrt{n_2(n_2-1)\cdots(n_2-4)} \\ &\qquad \times (n_3 + n_4 + 1). \end{aligned} \tag{29}$$

This and all other matrix elements were calculated with the help of symbolic calculus [34,58].

In addition to the selection rules for the atomic quantum numbers n_i, there are also selection rules for the angular momentum, and for the photon quantum number k. For unperturbed 2D helium, angular momentum is a conserved quantity, $\Delta l = 0$, though under the action of an electromagnetic field a state of angular momentum l is coupled to states of angular momentum $l-1$ or $l+1$, i.e., $\Delta l = \pm 1$. Therefore, with Eq. (26), each selection rule $\{\Delta n_1, \Delta n_2, \Delta n_3, \Delta n_4\}$ satisfies either $\Delta n_1 - \Delta n_2 + \Delta n_3 - \Delta n_4 = \pm 4$ or $\Delta n_1 - \Delta n_2 + \Delta n_3 - \Delta n_4 = 0$. From Eq. (17) we see that the operators T, V, and B (which are also operators of the unperturbed eigenvalue problem) do not couple states of different k values—only the field operator $\mathcal{F}(\theta)$ couples states where k changes by ± 1. Therefore, the selection rules for k are again $\Delta k = 0, \pm 1$. Furthermore, $\Delta k + \Delta l$ can only be equal to $0, 2$, or -2, thus $k + l \bmod 2$ is a conserved quantity.

F. Remaining symmetries

The basis set (28) does not yet account for the symmetries of the system, and, therefore, must be appropriately symmetrized. The Hamiltonian of the field-free atom commutes with the angular momentum L_z, and is invariant under rotations around a perpendicular axis z, under the parity Π operation ($[x,y,z] \to [-x,-y,-z]$), under the exchange operation P_{12}, and under the reflections Π_x and Π_y with respect to the coordinate axes x and y, respectively. Additionally, the representation in parabolic coordinates introduces nonphysical symmetries induced by the two-fold coordinate transformation [Eqs. (12) and (13)] [34,54]. The symmetrized basis adapted for P_{12} and L_z is defined by [34,54]

$$|n_1 n_2 n_3 n_4\rangle^+ = |n_1 n_2 n_3 n_4\rangle + |n_3 n_4 n_1 n_2\rangle, \tag{30}$$

with $n_1 - n_2 + n_3 - n_4 = 4L_z$ and $n_1 - n_2 \equiv n_3 - n_4 \equiv c_{12} \bmod 4$ ($c_{12}=0$ for singlet states, and $c_{12}=2$ for triplet states).

Under external driving, the 2D helium atom is no more invariant under rotations around a perpendicular axis z, and its Hamiltonian (1) is not invariant under the parity Π operation. Therefore, the only remaining symmetries are P_{12} and Π_x—provided the field is polarized along the x axis. Since $\Pi_x L_z = -L_z \Pi_x$, the basis elements (30) are not eigenstates of Π_x. Though the basis elements

$$|n_1 n_2 n_3 n_4\rangle^{+\epsilon_x} = |n_1 n_2 n_3 n_4\rangle^+ + \epsilon_x |n_2 n_1 n_4 n_3\rangle^+, \tag{31}$$

where $\epsilon_x = \pm 1$, are, with eigenvalue ϵ_x, and, therefore, account for the symmetries of the driven atom.

To conclude this section, let us remark that the basis (31) can also be used to represent the unperturbed 2D helium atom. In that case, for given values of P_{12}, Π_x, and $L_z^2 = l^2$, the eigenfunctions $|\psi_E\rangle$ corresponding to a given energy are superpositions of eigenfunctions with $L_z = l$ and $L_z = -l$, by virtue of Eqs. (31) and (26).

III. NUMERICAL TREATMENT

The representation of the time-independent set of coupled equations (17) in the basis set (31) leads to a generalized eigenvalue problem,

$$\mathcal{A}\mathcal{X}_i = \varepsilon_i \mathcal{B}\mathcal{X}_i, \tag{32}$$

in both, the driven and the unperturbed case. Due to the finite number of selection rules in the basis (31), $\mathcal{A}$ and $\mathcal{B}$ are infinite sparse banded matrices which have the following general form:

$$\mathcal{A} = \begin{pmatrix} \ddots & \vdots & \vdots & \vdots & \\ \cdots & \mathcal{H}_\alpha^{(k-1)}(\theta) & \eta\mathcal{F}_\alpha(\theta) & 0 & \cdots \\ \cdots & \mathcal{F}_\alpha(\theta) & \mathcal{H}_\alpha^{(k)}(\theta) & \eta\mathcal{F}_\alpha(\theta) & \cdots \\ \cdots & 0 & \mathcal{F}_\alpha(\theta) & \mathcal{H}_\alpha^{(k+1)}(\theta) & \cdots \\ & \vdots & \vdots & \vdots & \ddots \end{pmatrix}, \tag{33}$$

and

$$\mathcal{B} = \begin{pmatrix} \ddots & \vdots & \vdots & \vdots & \\ \cdots & B & 0 & 0 & \cdots \\ \cdots & 0 & B & 0 & \cdots \\ \cdots & 0 & 0 & B & \cdots \\ & \vdots & \vdots & \vdots & \ddots \end{pmatrix}, \tag{34}$$

with $\mathcal{H}_{\alpha}^{(k)}(\theta) = -Te^{-2i\theta}/2\alpha^8 + Ve^{-i\theta}/\alpha^4 - k\omega B$. $\mathcal{X}_i$ is the column vector which represents $|\phi_{\varepsilon_i}^k\rangle$, with $k \in \mathbb{Z}$.

The basis set (31) decomposes into the subspaces of singlet or triplet states, and of even or odd states with respect to the symmetry Π_x, with the following identification:

$$\begin{cases} \epsilon_x = \pm 1, & \text{even or odd states with respect to } \Pi_x, \\ n_1 - n_2 \equiv n_3 - n_4 \equiv 0 (\text{mod } 4), & \text{singlet states}, \\ n_1 - n_2 \equiv n_3 - n_4 \equiv 2 (\text{mod } 4), & \text{triplet states}. \end{cases} \tag{35}$$

However, due to the twofold symmetrization [Eq. (30) followed by Eq. (31)] of the basis, each element of the symmetrized basis can be represented by four quadruplets (n_1,n_2,n_3,n_4), (n_2,n_1,n_4,n_3), (n_3,n_4,n_1,n_2), and (n_4,n_3,n_2,n_1), and only one of them must be contained in the basis. Nevertheless, the basis can be defined unambiguously for $\epsilon_x = 1$, if each quadruplet (n_1,n_2,n_3,n_4) satisfies one of the following conditions:

$$\begin{cases} l > 0 & \text{and } n_1 \geq n_3, \\ l = 0, & n_1 > n_3, \quad \text{and} \quad n_1 \geq n_4 > n_2, \\ & n_1 > n_3 \quad \text{and} \quad n_1 > n_2 > n_4, \\ & n_1 > n_3 \quad \text{and} \quad n_1 = n_2, \\ & n_1 = n_3 \quad \text{and} \quad n_2 > n_4, \\ & n_1 = n_3 = n_2 = n_4. \end{cases} \tag{36}$$

For the basis which spans the odd subspace with respect to the x axis ($\epsilon_x = -1$), the basis states are defined by the same conditions, but states with $n_1 = n_2 = n_3 = n_4$ are forbidden [see Eq. (31)].

Under external driving, the angular momentum projection L_z is no more a conserved quantity. However, as we have seen in the previous section, $(k+l) \bmod 2$ is conserved. Therefore, also for the driven case, the space can be decomposed into even and odd subspaces, with respect to the generalized parity $\Pi_{kl} = (-1)^{k+l}$.

For our numerical implementation, the infinite symmetrized basis set also needs to be truncated. In the unperturbed case, we truncate the basis for a given angular momentum l according to

$$n_1 + n_2 + n_3 + n_4 \leq n_{\text{base}}, \tag{37}$$

with n_{base} a given positive integer. In the driven case, we additionally have to truncate the angular momentum and the photon number:

$$|l| \leq l_{\max} \quad \text{and} \quad k_{\min} \leq k \leq k_{\max}, \tag{38}$$

with positive integers $l_{\max}$, $k_{\min}$, and $k_{\max}$.

This representation at last leads to sparse banded matrices $\mathcal{A}$ and $\mathcal{B}$ in Eq. (32), with typically huge dimensions (e.g., $119\,460 \times 6662$ for the description of the spectrum of field-free 2D helium above the 15th ionization threshold, or $521\,795 \times 50\,717$ for the description of the Floquet spectrum of the near-resonantly driven frozen planet configuration in the 6th autoionization channel—see Secs. IV and V). The numerical diagonalization of Eq. (32) combines the Lanczos algorithm [59–61] and advanced techniques of parallel programming [34,62–64], and was carried out on large computers like the HITACHI SR8000-F1 of the Bavarian Academy of Sciences [97], and the IBM p690 of the Max Planck Society [98].

Finally, together with the rotation of configuration space by an angle θ, we also introduce a dilation by a positive real number α_c, such that the (Cartesian) coordinates and momenta transform according to $\boldsymbol{r} \to \alpha_c \boldsymbol{r} e^{i\theta}$ and $\boldsymbol{p} \to \boldsymbol{p} e^{-i\theta}/\alpha_c$. Since the dilation by a factor α_c is a unitary transformation described by the unitary operator [56,65]

$$D_{\alpha_c} = \exp\left(i(\ln \alpha_c) \frac{\boldsymbol{r}\cdot\boldsymbol{p} + \boldsymbol{p}\cdot\boldsymbol{r}}{2} \right), \tag{39}$$

the spectra of a Hamiltonian H and of the dilated Hamiltonian $H_{\alpha_c} = D_{\alpha_c} H D_{\alpha_c}^{\dagger}$ are the same. However, when the basis is truncated, the spectrum *does* depend on the parameter α_c if the basis set is not large enough. Therefore, α_c can be used as a variational parameter that has to be optimized. Additionally, we note that a dilation by α_c in Cartesian coordinates is equivalent to a dilation by $\alpha_c^{1/4}$ in parabolic coordinates, since the former are homogeneous polynomials of 4th degree in the latter. In the sequel we always refer to the dilation parameter in parabolic coordinates, $\alpha = \alpha_c^{1/4}$.

IV. SPECTRUM OF 2D HELIUM

As in the three-dimensional case [6], the eigenstates of 2D helium are organized in Rydberg series converging to single ionization thresholds which all converge to the double ionization threshold at zero energy. The threshold structure of the spectrum is essentially the same as for the case without electron-electron interaction, and the location of the various single ionization thresholds is unaffected by the term $1/r_{12}$, since the electron interaction vanishes at large distances. Thus, the Nth threshold energy is given by [34,54]

$$I_N = -\frac{Z^2}{2(N - 1/2)^2}, \quad N \geq 1 \text{ integer}, \tag{40}$$

a series which obviously converges to zero with $N \to \infty$.

A. Discrete spectrum

The first series of eigenenergies converges to the threshold $I_1 = -8$ a.u., and above this energy all bound states with $N > 1$ are embedded into the continuum of lower series, i.e., they are resonance states with finite width [53]. The spectrum can be classified by the particle exchange symmetry, the symmetry Π_x with respect to the x axis, and the absolute value $|l|$ of the angular momentum (or, equivalently, l^2).

The ground-state energy of 2D helium is found for $|l| = 0$, singlet, and $\Pi_x = +1$ symmetry. With $Z = 2$, $\gamma = 1$,

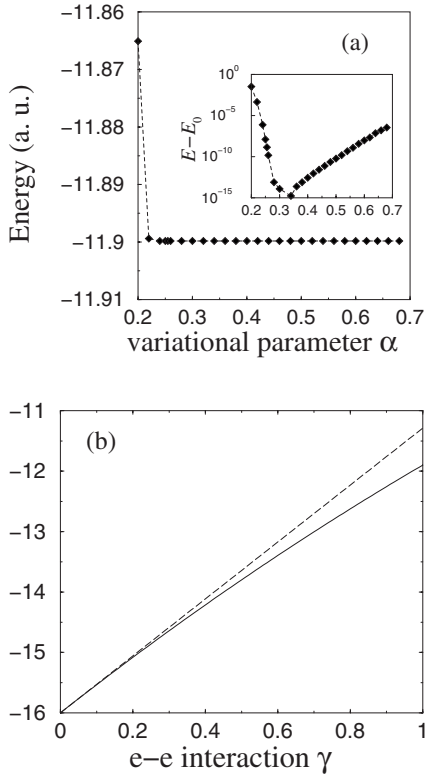

FIG. 1. Dependence of the ground-state energy of the 2D helium atom ($\gamma=1$) in atomic units, on the dilation parameter α, for $n_{\text{base}}=60$ (a), and ground-state energy in a.u. as a function of the strength γ of the electron-electron interaction (b). In (b), the dashed line is obtained from first-order perturbation theory, while the solid line represents our numerical results. The inset in (a) zooms into the apparent plateau of E vs α, in the vicinity of the actual minimum value of E at $\alpha \simeq 0.36$.

$n_{\text{base}}=60$ (what generates matrices with $n_{\text{tot}}=816$ elements on the main diagonal), we obtain

$$E_0 = -11.899\,822\,342\,953 \text{ a.u.}$$

For the numerical calculation of the ground state (and in general of any bound state of the first series of Rydberg states) we do not need to use complex rotation (i.e., we can set $\theta=0$), since there is no open decay channel. However, due to the truncation of the basis, the energy depends on the dilation parameter α. The variational character of α can be appreciated from Fig. 1(a), where the dependence of the energy of the 2D He ($Z=2$, $\gamma=1$) ground state on α is illustrated for $n_{\text{base}}=60$ ($n_{\text{tot}}=816$). For $0.26 \leq \alpha \leq 0.5$, the numerical values are stable, and for $\alpha \simeq 0.36$ the curve has a minimum [see the inset in Fig. 1(a)]. In Fig. 1(b) we corroborate the linear behavior of the energy of the ground state of the 2D problem as a function of the strength γ of the electron-electron interaction, as predicted by first-order perturbation theory, for sufficiently small values of γ ($\gamma \leq 0.3$).

The energy levels for l and $-l$ ($l>0$) are degenerate, what further implies the degeneracy of $\Pi_x=+1$ and $\Pi_x=-1$ for given $|l|>0$. This degeneracy is confirmed in Table I for the singlet $|l|=1$ energy levels below the first ionization threshold.

TABLE I. Singlet energy levels below the first ionization threshold for $|l|=1$ and $\Pi_x=\pm 1$, in atomic units. Basis truncation $n_{\text{base}}=250$ [see Eq. (37)]. The total size of the basis is 84 320, for both $\Pi_x=-1$ and $\Pi_x=+1$. Optimal value of the scaling parameter: $\alpha=0.40\pm0.02$.

$\Pi_x=+1$	$\Pi_x=-1$
−8.211 542 089 886	−8.211 542 089 886
−8.077 637 328 985	−8.077 637 328 985
−8.039 947 879 467	−8.039 947 879 467
−8.024 280 94	−8.024 280 94
−8.016 303 52	−8.016 303 52
−8.011 69	−8.011 69

In the absence of the electron-electron interaction, the zero angular momentum energy levels below the first ionization threshold are doubly degenerate (except for the ground state), with one singlet state and one triplet state. Moreover, all these states have symmetry $\Pi_x=+1$. In the 2D helium atom the interelectronic repulsion breaks this degeneracy. The degenerate levels for $\gamma=0$ split in two distinct levels for $\gamma>0$, one singlet state and one triplet state, both with $\Pi_x=+1$ symmetry. This can be understood if we consider the limit $\gamma=0$: the eigenstates of the noninteracting problem can be labeled by the principal quantum numbers $N_1^{(0)}$, $N_2^{(0)}$ ($N_i^{(0)} \geq 1$), and by the angular momenta L_1, L_2 ($-N_i^{(0)}+1 \leq L_i \leq N_i^{(0)}-1$) of the electrons. Therefore, symmetrized zero angular momentum states are of the form $|N_1^{(0)}, N_2^{(0)}, L, -L\rangle^{\epsilon_x} = |N_1^{(0)}, N_2^{(0)}, L, -L\rangle + \epsilon_x |N_1^{(0)}, N_2^{(0)}, -L, L\rangle$, with $\epsilon_x=+1$ ($\epsilon_x=-1$) for symmetric (antisymmetric) states with respect to Π_x. In particular, zero angular momentum states of the first series carry the labels $|1, N_2^{(0)}, 0, 0\rangle$ and $|N_2^{(0)}, 1, 0, 0\rangle$. Therefore, there are no $\Pi_x=-1$ eigenstates below the first ionization threshold. Since the electron-electron interaction does not break the Π_x symmetry, the latter result remains valid for any value of γ. Furthermore, we numerically verified that, for $|l|=0$ and $\Pi_x=-1$, there are no bound states below I_1 and, *a forteriori*, no continuum states attached to this threshold. This implies that the lowest eigenenergies for this symmetry correspond to bound states. Indeed, all $\Pi_x=-1, |l|=0$ eigenstates of 2D helium below the second ionization threshold are bound, and in Table II we summarize the lowest energy levels of this series.

TABLE II. Lowest *bound* energy levels below the second ionization threshold for $\Pi_x=-1$ and $|l|=0$, in atomic units. N and n label the excitation of the inner and of the outer electron, respectively. The truncation parameter was chosen as $n_{\text{base}}=200$, and the optimal scaling parameter is $\alpha=0.40\pm0.02$.

N	n	Triplet states	Singlet states
2	2	−1.273 641 219 559	
2	3	−0.984 664 061 020	−1.003 293 436 315
2	4	−0.934 882 211 552	−0.940 478 975 302
2	5	−0.915 916 000 683	−0.918 334 694 991
2	6	−0.906 668 776 66	−0.907 931 197 24

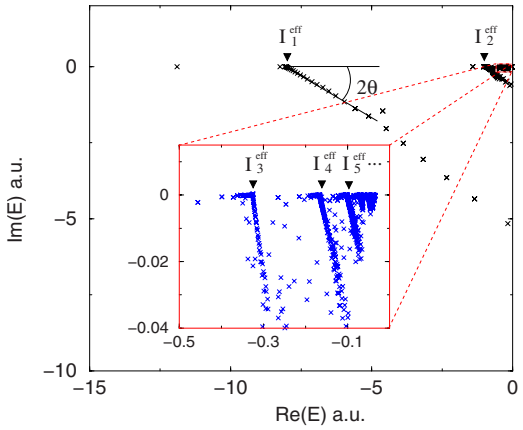

FIG. 2. (Color online) Complex energy spectrum of the rotated 2D helium Hamiltonian (2), for singlet states, $\Pi_x=+1$, and $|l|=0$. The data were obtained by several runs of the Lanczos algorithm, choosing the shift parameter [34,62] close to the ionization thresholds I_N, $N=1\cdots5$. Due to the truncation of the basis, $I_N^{\text{eff}}<I_N$ [66]. In all cases $\theta=0.3$, while the parameters α and n_{base} have to be readjusted to obtain optimal convergence in the different spectral ranges. For the eigenvalues above the sixth ionization series we used $n_{\text{base}}=300$, what implies a basis size of 76 076.

A complete description of the spectrum below the first ionization threshold can be found in [54]. There, the energy levels below the first ionization threshold are labeled by the principal quantum number n of the outer electron, as if the electrons were noninteracting. This picture can also be extended to moderately doubly excited states, where the quantum number N of the inner electron labels its Rydberg level, equivalent to the single ionization thresholds.

B. Resonance spectrum

For the description of the resonance spectrum above the first ionization threshold we use complex rotation, and thus, besides the scaling parameter α, also need to adjust the rotation angle θ to achieve optimal convergence. A typical spectrum of the rotated Hamiltonian of field-free 2D helium is shown in Fig. 2, for singlet states with $\Pi_x=+1$, and zero angular momentum. One clearly observes the continuum part of the spectrum rotated by an angle close to 2θ into the lower half of the complex plane, around the single ionization thresholds $I_1, I_2, \ldots, I_5, \ldots$. Indeed, due to the truncation of the basis, the exact thresholds cannot be reached, but only effective ionization thresholds I_N^{eff} [62,66]. The doubly excited states appear as isolated complex eigenvalues: the real part is the energy E of the resonance, and the imaginary part equals $-\Gamma/2$, with Γ the decay rate.

The first resonance of 2D helium is found for zero angular momentum and singlet exchange symmetry. The complex eigenvalue of this resonance state is

$$E = -1.411\,496\,328\,143 - i\,0.001\,241\,734\,389 \text{ a.u.}$$

It is obtained for the parameters $\theta\simeq0.4$, $\alpha\simeq0.35$, $n_{\text{base}}=200$, and a basis size 23 426. For triplet exchange symmetry the lowest resonance is found for $|l|=1$, and its energy

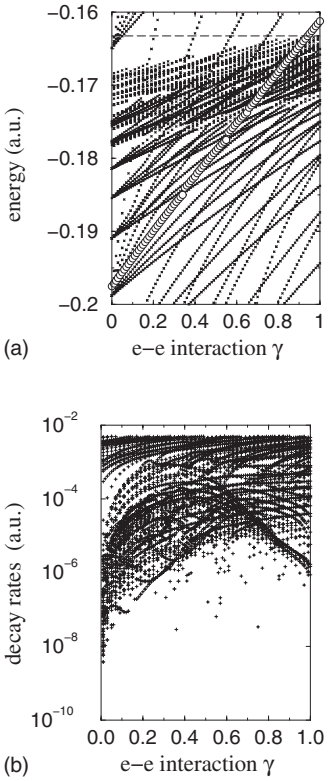

FIG. 3. Energies (a) and decay rates (b) of the resonances of the 2D three-body problem, as a function of γ for singlet exchange symmetry, $\Pi_x=+1$, and $|l|=0$, close to the 4th helium ionization threshold ($I_4=-8/49$ a.u.). The lowest resonance (◦) of the 5th Rydberg series exhibits several avoided crossings before crossing the 4th ionization threshold (indicated by the long dashed line), with associated dramatic enhancements of its decay rate at the crossings (note the logarithmic scale of the right-hand plot).

and decay rate are $E=-1.386\,1382\,101\,96$ a.u. and $\Gamma/2=0.000\,056\,648\,625$ a.u., respectively.

The degeneracy of the energy levels of 2D helium without electron-electron interaction (i.e, two coupled 2D hydrogen atoms) is $2(2N_1^{(0)}-1)(2N_2^{(0)}-1)$, if $N_1^{(0)}\neq N_2^{(0)}$, or $(2N_1^{(0)}-1)^2$, if $N_1^{(0)}=N_2^{(0)}$. The factor 2 in the $N_1^{(0)}\neq N_2^{(0)}$ case stems from the particle exchange symmetry. In particular, the lowest excited state $(E_{N_1^{(0)}=N_2^{(0)}=N})$ of the Nth zero angular momentum Rydberg series is $(2N-1)$-fold degenerate.

These simple considerations already impressively illustrate the dramatic enhancement of the density of states as we increase the electronic excitation. Figure 3 depicts the level and decay rate dynamics in the vicinity of the 4th ionization threshold. In the perturbative regime of small γ values we observe a linear behavior of the energy levels, while the decay rates grow proportionally to γ^2, in agreement with perturbation theory for degenerate states [67]. Such behavior prevails for the lowest lying resonances, over a large range of γ. However, for higher excitations, different resonances start to interact, and deviations from the perturbative regime are observed.

For highly excited states, different Rydberg series overlap, what again enhances the density of states, and thus multiplies the incidences of resonance interaction. At $\gamma=0$, the energy

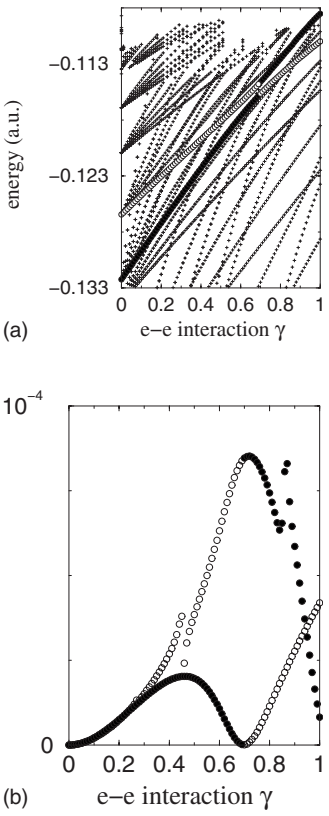

FIG. 4. Energy (a) and decay rate (b), in atomic units, of the lowest resonance $N=6,n=6$ (•) of the 6th Ryberg series for singlet exchange symmetry, $\Pi_x=+1$, and $|l|=0$, under variation of the electron-electron interaction γ. This resonance exhibits a clear avoided crossing with one of the $N=4,n=9$ resonances (◦), at $\gamma \simeq 0.7$, where its decay rate is dramatically reduced.

level $E_{N=5,n=5}=-(16/81)$ a.u$\simeq -0.1975$ a.u. lies below the 4th ionization threshold $I_4=-(8/49)$ a.u.$\simeq -0.1633$ a.u: Hence, the 4th and the 5th Rydberg series overlap. We identify the diabatic continuation of $E_{N=5,n=5}$ by its maximal overlap with the original eigenstate at $\gamma=0$, leading to the energy levels progression marked by ◦ in Fig. 3. Closer inspection of the spectral structure in the regime of highly doubly excited states shows that the level dynamics is governed by avoided crossings [68–70] which stem from the coupling induced by the *e-e* interaction. In particular, before evolving into the lowest resonance of the 5th series of 2D He ($\gamma=1$), the continuation of the $N=5,n=5,\gamma=0$ state exhibits several avoided crossings, due to the high density of states close to the ionization threshold. Finally, it *crosses* the 4th ionization threshold at I_4, and only then settles into the corresponding He state.

The situation for the lowest resonance of the 6th series is a little bit different, as illustrated in Fig. 4. In this case the resonance starts at the energy level $E_{N=6,n=6}=-(16/121)$ a.u.$\simeq -0.1322$ a.u., which is far below the next ionization threshold at $I_5=-(8/81)$ a.u.$=-0.0988$ a.u. In this energy range the number of interacting states is reduced, and the state exhibits a prominent avoided crossing before it settles into the corresponding 2D He state. The interaction at $\gamma \simeq 0.7$ with one of the $N=4$, $n=9$ resonances, marked with open circles (◦), dramatically suppresses its decay rate (right plot) to values close to zero (9×10^{-8} a.u.). This behavior is strongly reminiscent of a quasibound state in the continuum [71].

TABLE III. Lowest energy levels and decay rates of doubly excited helium states, for vanishing angular momentum, singlet exchange symmetry, and $\Pi_x=+1$, up to the 7th series. For the higher excitations we used $n_{\text{base}}=300$, with a basis size 76 076. The relatively poor convergence of the 5th state is due to its interaction with the rotated continuum emanating from the I_4 threshold [see also Fig. 3 (a), at $\gamma=1$].

N,n	I_N	Energy (a.u.)	$\Gamma/2$ (a.u.)
2,2	−0.88889	−1.411 496 328 143	−0.001 241 734 389
3,3	−0.32000	−0.516 872 103 407	−0.001 165 786 319
4,4	−0.16327	−0.265 531 275 47	−0.000 774 567 15
5,5	−0.09877	−0.161 223 759	−0.000 572 27
6,6	−0.06612	−0.108 510 920 110	−0.000 008 262 814
7,7	−0.04734	−0.077 577 461 413	−0.000 044 363 709

In Table III we show the converged energy levels and decay rates of the lowest doubly excited states, up to the 7th Rydberg series. All these resonances are found for singlet exchange symmetry, $\Pi_x=+1$, and $|l|=0$. We see that the lowest resonance of the 6th series lies below the 5th ionization threshold I_5. Hence, the 5th Rydberg series overlaps with the 6th series of the 2D helium atom. Similarly, the 6th and the 7th series overlap, and so forth. Thus, starting at the 5th series, all series mix.

V. THE 2D FROZEN PLANET CONFIGURATION

A. The unperturbed frozen planet

In the frozen planet configuration (FPC) [16] both electrons are located on the same side of the nucleus, with asymmetric excitation. On a first glance, this highly asymmetric structure might appear to be unstable. However, classical studies [72–74] show that, indeed, it is *dynamically stable*: while the inner electron follows highly eccentric elliptic trajectories which precess around the symmetry axis of the configuration, the outer electron is localized around some equilibrium distance far from the inner electron. It is dynamically stabilized due to the fast oscillation of the latter, which implies a rapidly oscillating potential experienced by the outer electron, due to the competition between the electron-electron repulsion and the Coulomb attraction exerted on the outer electron by the screened Coulomb potential of the nucleus. Upon averaging [47] over the characteristic time scale of the inner electron's motion, the outer electron experiences an effective, time-independent, weakly attractive potential which determines the equilibrium distance [75]. Indeed, the existence of these configurations was shown by accurate 3D [76] and 1D [20] quantum calculations, originally triggered by earlier laboratory experiments [77].

Starting from the third series ($N=3$) of the 2D helium spectrum we have identified quantum states which are localized on the FPC. These are organized in subseries converging to the respective single ionization thresholds, and typi-

TABLE IV. Energies and decay rates of the fundamental ($n_F=1$) singlet (^1S) and triplet (^3S) frozen planet states (FPS) below the Nth single ionization threshold. For the accurate numerical calculation of the $N=14$, $n_F=1$ FPS the optimal parameters were $\alpha \simeq 0.5$, $\theta \simeq 0.25$, and $n_{\text{base}}=350$ (producing banded matrices of dimension $119\,460 \times 6662$). All values are in a.u.

N	$E^{(2D)}(^1S)$	$E^{(2D)}(^3S)$	$(\Gamma/2)^{(2D)}(^1S)$	$(\Gamma/2)^{(2D)}(^3S)$
3	−0.354 907 546	−0.352 128 586	0.000 003 372	0.000 001 529
4	−0.180 560 506	−0.180 360 429	0.000 000 877	0.000 000 418
5	−0.109 297 550	−0.109 260 500	0.000 003 748	0.000 000 021
6	−0.073 207 046	−0.073 203 013	0.000 010 180	0.000 000 005
7	−0.052 445 661	−0.052 443 726	0.000 001 443	0.000 000 129
8	−0.039 408 949	−0.039 408 949	0.000 000 317	0.000 000 31
9	−0.030 693 094	−0.030 693 093	0.000 000 158	0.000 000 390
10	−0.024 578 744	−0.024 578 820	0.000 000 087	0.000 000 037
11	−0.020 125 003	−0.020 125 045	0.000 000 105	0.000 000 016
12	−0.016 780 71	−0.016 780 695	0.000 000 03	0.000 000 007
13	−0.014 205 703	−0.014 205 698	0.000 000 006	0.000 000 003
14	−0.012 180 962	−0.012 180 961	0.000 000 002	0.000 000 001

cally exhibit small decay rates, as compared to other eigenstates. Therefore, each frozen planet state (FPS) can be labeled by the excitation N of the inner electron, and by a quantum number n_F which refers to its position within the associated subseries converging to I_N. In Table IV we summarize the energies and decay rates of the lowest ($n_F=1$) singlet (^1S) and triplet (^3S) FPS of the subseries converging to the Nth ionization threshold, for $N=3,4,\ldots,14$.

While the role of the dimension of configuration space for the characteristic properties (lifetimes and energies) of the FPS was discussed in [24], we focus here on the localization properties of 2D FPS in configuration and phase space: When restricted to the collinear FPC, the classical two-electron dynamics is regular [see Fig. 5(a)] [5,73]. Furthermore, the equilibrium distance $x_{\min}$ of the outer electron to the nucleus, as well as the minimum E_N of the effective potential can be expressed in terms of the principal quantum number N of the inner electron, as a consequence of the scale invariance (3) and (4) of the classical equations of motion. Also the maximum static field strength F_I that can be applied to the configuration without ionizing it, and the frequency ω_I of small oscillations around the equilibrium point can be expressed as function of N. Altogether we have

$$x_{\min} = 2.6(N-0.5)^2, \tag{41}$$

$$E_N = -2.22(N-0.5)^{-2}, \tag{42}$$

$$\omega_I = 0.3(N-0.5)^{-3}, \tag{43}$$

$$F_I = 0.03(N-0.5)^{-4}. \tag{44}$$

The mapping of FPS wave functions on the classical phase space is achieved with the projective Husimi distributions described in Appendix Sec. 2. Figure 5 shows the phase space projections of the first three FPS of the sixth triplet series in comparison to the Poincaré surface of section of the FPC. The localization of the frozen planet states is apparent in these plots: while the fundamental state of the series is well localized on the regular frozen planet periodic orbit, at the minimum of the effective potential at 2.6 scaled units, excited states are localized along frozen planet trajectories well identified by the position of the maximum in the Husimi function at the outer turning point of the classical orbit.

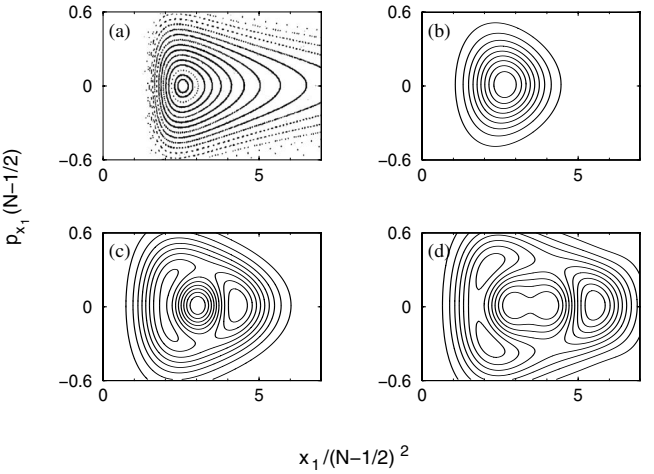

FIG. 5. Contour plots of the Husimi representation of the $n_F=1$ (b), $n_F=2$ (c), and $n_F=3$ (d) triplet frozen planet states (FPS) of the sixth series, compared with the classical phase space of the collinear frozen planet configuration (FPC) in (a) [16,73]. The Husimi functions show perfect phase space localization: while the fundamental state (a) is localized at the minimum of the effective potential, at 2.6 scaled units [20,75], the excited states are localized along frozen planet trajectories with higher energy, with outer turning points (at the maxima of the Husimi densities) at 4.2 (c) and 5.5 (d) scaled units.

This is also spelled out by the configuration space representation of the electronic density in Fig. 6 (see Appendix Sec. 1 for technical details). The electrons are localized at different regions of space: The maximum in the radial distance r_2 of the inner electron remains invariant for all excited states, what shows that the excitation of the inner electron (i.e., the quantum number N) remains invariant. On the other hand, the density of the outer electron peaks at different radial distances r_1, and this distance increases with n_F. Thus, n_F is a quantum number that labels the excitation of the outer electron. This is, additionally, reflected in the nodal structure of the wave functions (along r_1).

B. The resonantly driven frozen planet

Apart from its independent interest for the field free, autonomous helium problem already discussed above, the frozen planet configuration is of potentially high relevance in the context of coherent control [78–80] in the electronic dynamics of Rydberg systems in the presence of electron-electron interactions [81]: During the last decade, it has been realized that near-resonant electromagnetic driving of atomic electrons in one-electron Rydberg systems allows to create *nondispersive electronic wave packets* [82–85] (in a quantum

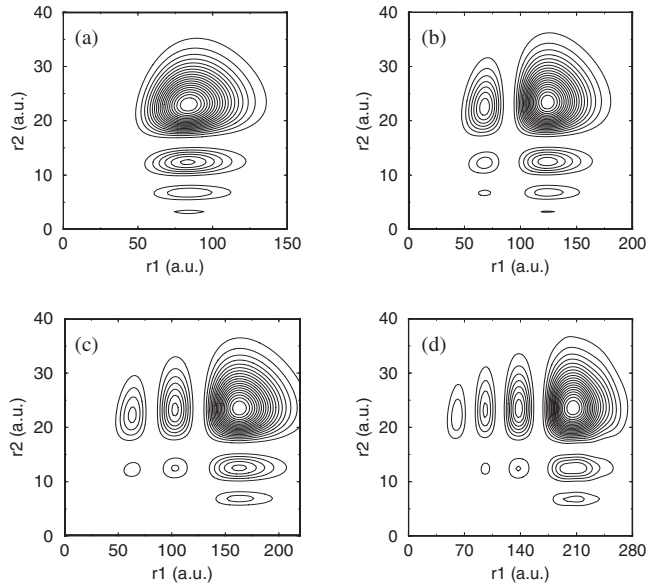

FIG. 6. Conditional probability densities (with a fixed interelectronic angle $\theta_{12}=0$) of the first four triplet frozen planet states (FPS) of the sixth series ($N=6$): (a) $n_F=1$; (b) $n_F=2$; (c) $n_F=3$; (d) $n_F=4$. The maxima of the electronic densities in the radial distance r_2 of the inner electron remain invariant, while the most likely position of the outer electron (at the outer turning point of its classical orbit) increases with n_F. The number of nodes in the radial coordinate r_1 is precisely given by n_F-1.

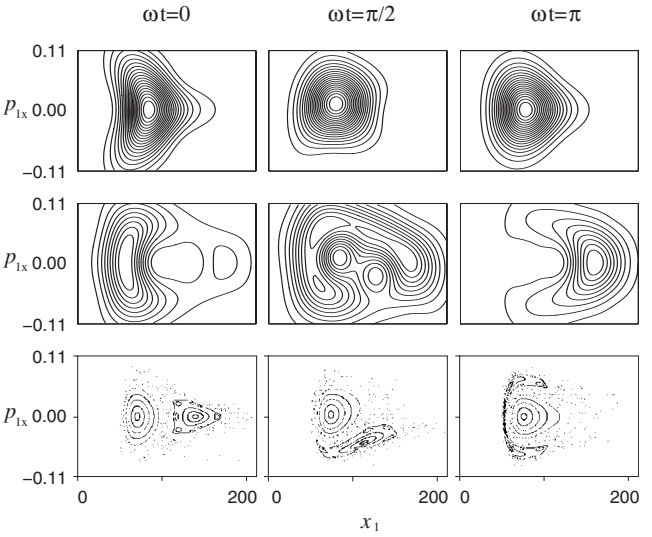

FIG. 7. Contour plot of the Husimi distribution (A13) of two different wave-packet triplet eigenstates (top and middle) along a $N=6$ frozen planet trajectory of 2D helium, under electromagnetic driving at frequency $\omega=0.0012$ a.u. and amplitude $F=5.5\times10^{-6}$ a.u., projected onto the phase space component spanned by x_1 and p_1 (the position and momentum of the outer electron). For comparison, also the classical phase space structure of the restricted collinear problem [20] is shown (bottom), for the same driving field parameter. Clearly, the electronic density is associated with the chaotic phase space region, and is localized around the hyperbolic fix point of the 1:1 resonance.

system with a *nonharmonic* spectrum) which propagate along Kepler trajectories of essentially arbitrary eccentricity and orientation for very long times [19,82,85]. This field has by now been investigated theoretically in much detail and is well understood, and first experimental realizations of such long living "quantum particles" have been reported very recently [22,86–89]. An immediate question is of course whether such a localization and stabilization effect is also to be expected in systems with additional electron-electron interaction, e.g., in helium. Indeed, two-electron wave packets have been experimentally prepared in barium atoms, though eventually dispersed [90]. Furthermore, diffusion Monte Carlo calculations suggest that circularly polarized electromagnetic *together with* static magnetic fields can prevent two-electron wave packets launched along *Langmuir orbits* from spreading [25]. As for the frozen planet configuration, it was shown that nondispersive two-electron wave-packet eigenstates which propagate along the frozen planet trajectory *do exist* in a one-dimensional model of helium [20,21,23], if an external oscillating field's frequency is tuned into resonance with the associated eigenfrequency (43). However, a demonstration of this stabilization effect beyond the 1D treatment was hitherto missing.

For our numerical investigation of the time evolution of frozen planet states under periodic driving we choose the field frequency $\omega=0.2(N-0.5)^{-3}$ a.u., close to the intrinsic frequency (43), and the field amplitude $F=0.005(N-0.5)^{-4}$ a.u. With these field parameters, a driving-induced 1:1 resonance island and an intrinsic island—the remainder of the regular phase space structure of the unperturbed configuration, see Fig. 5(a)—are very well distinguishable in the classical phase space dynamics. As observed in Fig. 7 (bottom) [20], the intrinsic regular island is centered around the equilibrium position of the configuration, and remains basically unaffected by the field, while the resonant island oscillates around the intrinsic island, under variation of the phase ωt of the drive.

In order to assess the effects of the near resonant driving on the quantum mechanical FPS, the eigenvalue problem (32) has to be solved. Since the frozen planet states emerge from the highly excited spectrum, we expect that semiclassical aspects can be imported. Indeed, the classical dynamics of the driven frozen planet suggest that the system decays via ionization of a single electron [20]. Therefore, we assume that single ionization is the dominant decay process, and only need to resolve the next higher single ionization threshold. This significantly reduces the size of the eigenvalue problem to be solved. For example, for $N=6$, the number of photons necessary to reach the next single ionization threshold $I_{N=6}$ from the $n_F=1$ FPS is four—in contrast to 61 photons that separate this state from the double ionization threshold.

However, even for small photon numbers, due to the periodicity of the Floquet spectrum, the local density of states increases dramatically as compared to the field-free case. For instance, the complex-valued Floquet resonance spectrum obtained by diagonalization of Eq. (17), for $k_{\min}=-2$, $k_{\max}=4$, $l_{\max}=3$, and near-resonant driving of the periodic orbits associated with the $N=6$ series ($\omega=0.0012$ a.u., and $F=5.5\times10^{-5}$ a.u.) is shown in Fig. 8. In such a spectrum, those eigenstates $|\psi\rangle$ emerging from the FPS $|\psi_{\mathrm{FPS}}\rangle$ of the field free

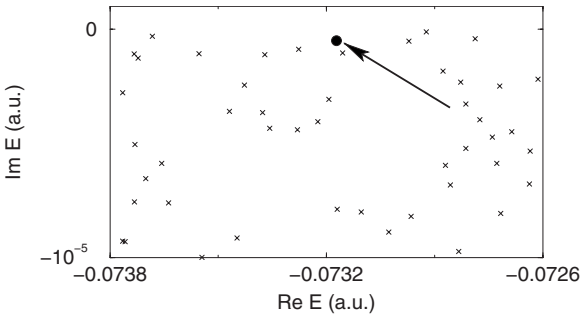

FIG. 8. Complex-valued Floquet spectrum of Eq. (17), for triplet states, within one Floquet zone of width ω. The real parts of the resonance poles (crosses) correspond to the energies, the imaginary parts to half the decay rates of the atomic resonance states in the field. The state highlighted by a black spot and an arrow at Re(E) $=-0.073\,172\,3$ a.u. exhibits the largest overlap with the third excited FPS of the $N=6$ series [see Fig. 5(d)]. $F=5.5\times10^{-6}$ a.u., $\omega=0.0012$ a.u., $n_{\mathrm{base}}=200$, 7 photon blocks, $k_{\mathrm{min}}=-2$, $k_{\mathrm{max}}=4$, $l_{\mathrm{max}}=3$, $n_{\mathrm{tot}}=521795$.

atom can be identified by inspection of the overlaps $|\langle\psi|\,\psi_{\mathrm{FPS}}\rangle|^2$. The state marked by a black spot in Fig. 8 shows the largest overlap, 83%, with the $N=6$, $n_F=3$ FPS of the unperturbed atom.

A direct comparison of the time evolution of the 2D Floquet states with the classical dynamics can be obtained from the projection of the outer electron's density on the phase component spanned by the symmetry axis of the configuration—which is fixed by the polarization axis of the driving field (along x). Technical details can be found in Appendix Sec. 4. Figure 7 shows the phase space projection of the triplet Floquet states with largest overlap with the $N=6$, $n_F=1$ (top), and $n_F=3$ (middle) FPS, for phases $\omega t=0$ (left), $\omega t=\pi/2$ (center), and $\omega t=\pi$ (right) of the driving field. The $n_F=1$ wave packet is rather uninteresting: it is localized on the intrinsic island, and almost unaffected by the driving field. However, the $n_F=3$ Floquet state is anchored to the unstable (hyperbolic) fix point of the 1:1 resonance and oscillates around the minimum of the effective potential of the field free atom, with no apparent dispersion in the x direction. There are also wave packets associated with the stable elliptic fix point of the resonance, though no converged triplet eigenstates of the $N=6$ series could be found. An example of such an elliptic wave packet is shown in Fig. 9, and was found below the singlet $N=6$ ionization threshold.

The electronic density of the above wave packet in configuration space (Figs. 10 and 11) reveals remarkably accentuated fingerprints of the different unperturbed FPS—which are now coupled coherently by the external field: the triplet wave packet reminds us of the $n_F=3$ FPS [see Fig. 6(c)] at phase $\omega t=0$, and of the $n_F=1$ FPS [see Fig. 6(a)] at $\omega t=\pi$ [Figs. 10(a1), 10(a2), 10(a3), 11(a1), 11(a2), and 11(a3)]. The influence of the external driving is particularly pronounced in the dynamics of the outer electron: the latter follows the oscillations of the field [Figs. 10(c1), 10(c2), 10(c3), 11(c1), 11(c2), and 11(c3)], while the inner electron remains unaffected [Figs. 10(b1), 10(b2), 10(b3), 11(b1), 11(b2), and 11(b3)].

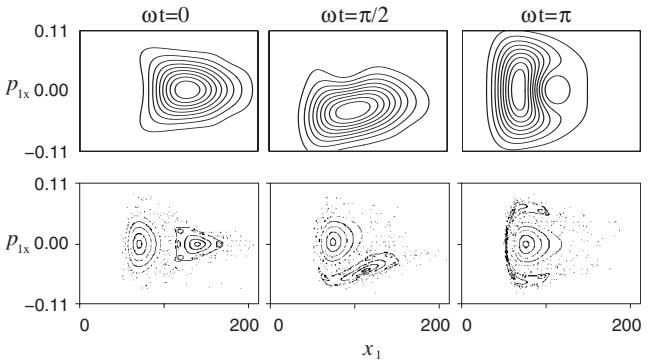

FIG. 9. Contour plot of the Husimi phase space distribution (A13) of the wave-packet singlet eigenstate (top) along a $N=6$ frozen planet trajectory of 2D helium, under electromagnetic driving at frequency $\omega=0.0012$ a.u. and amplitude $F=5.5\times10^{-6}$ a.u. The (restricted) phase space is spanned by the outer electron's position x_1 and momentum p_{x_1} along the driving field polarization axis. For comparison, also the classical phase space structure of the restricted collinear problem [20] is shown (bottom), for the same driving field parameters. The electronic density remains localized around the elliptic fix point of the driving-induced 1:1 resonance.

Figures 10 and 11 also highlight the multifaceted appearance of the electronic density, when represented in a two-dimensional plot: The localization properties of either one of the electrons are always conditioned on the other: While we fix the interelectronic angle $\theta_{12}=0$ in Fig. 10(a), we fix the outer electron's position at $x_1\simeq165$ a.u., $y_1=0$ in Fig. 10(b),

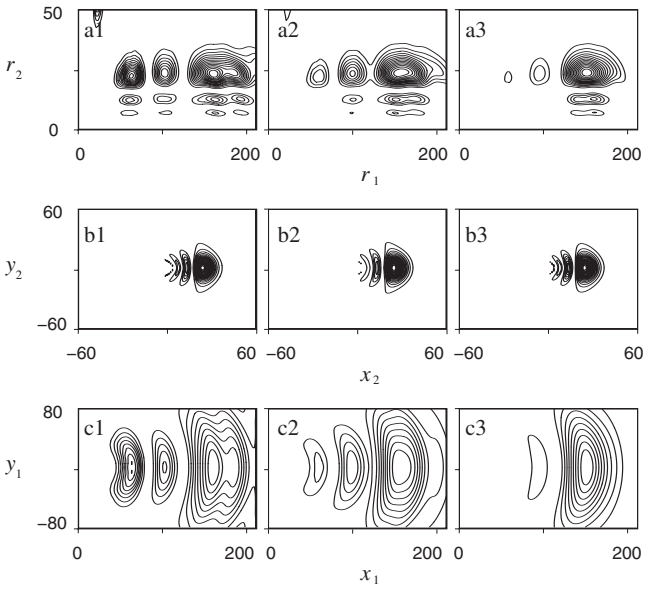

FIG. 10. Electronic density of the $N=6$ triplet wave packet (Fig. 7) in configuration space, for different phases of the driving field: $\omega t=0$ [(a1), (b1), (c1)], $\omega t=\pi/2$ [(a2), (b2), (c2)], $\omega t=\pi$ [(a3), (b3), (c3)]. (a1)–(a3) show the electronic density as a function of the distances r_1 and r_2 of the electrons from the nucleus, for fixed interelectronic angle $\theta_{12}=0$. (b1)–(b3) depict the electronic density of the inner electron, when the outer electron is fixed at a distance $r_1\simeq165$ a.u. along the x axis—its outer turning point in (a1)–(a3). In (c1)–(c3) the probability density of the outer electron is shown, for the inner electron fixed at $r_2\simeq23$ a.u. along the x axis.

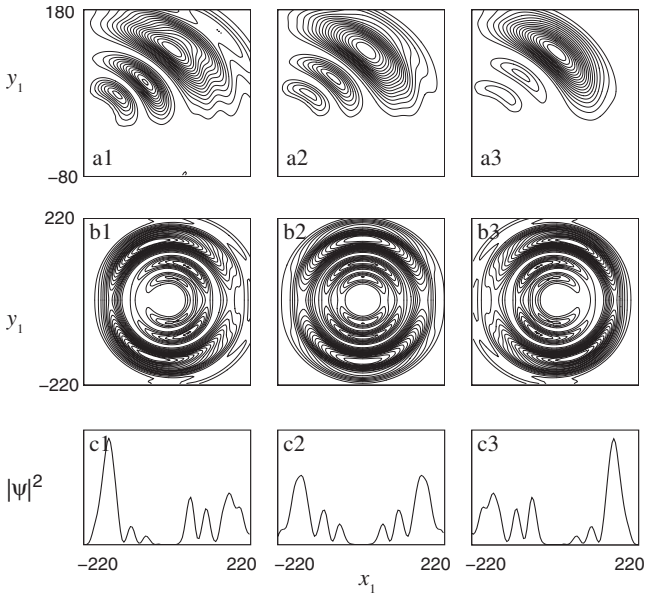

FIG. 11. Electronic density of the $N=6$ triplet wave packet (Figs. 7 and 10) in configuration space, for different phases of the driving field: $\omega t=0$ [(a1), (b1)], $\omega t=\pi/2$ [(a2), (b2)], $\omega t=\pi$ [(a3), (b3)]. (a1)–(a3) shows the electronic density of the outer electron for the inner electron fixed at a distance $r_2=23$ a.u. on the diagonal $y=x$. (b1)–(b3) represents the electronic density of the outer electron when the inner electron is delocalized over a circle with radius $r_2=23$ a.u. The x profiles of (b1)–(b3) are shown in (c1)–(c3).

and the inner electron at $x_2 \simeq 23$ a.u., $y_2=0$ in Fig. 10(c). Figure 11(a) shows that the outer electron's transverse localization is only weakly spreading as we displace the inner electron's initial condition from the field polarization axis, and exhibits the same dependence on ωt. Figures 11(b) and 11(c) are finally obtained for an arbitrary angular position of the inner electron on a circle of radius 23 a.u.. Correspondingly, also the outer electron's angular position is distributed over the entire circle, though with a clear time-dependent modulation in phase with the driving field.

Despite the impressive size of the basis used in the diagonalization of the eigenvalue problem (521 795 basis elements) we have not been able to obtain a converged value of the lifetime of this wave packet. Our numerical analysis suggests a lifetime $\Gamma^{-1} \geq 100 \times 2\pi/\omega$, which is already satisfactory for standard wave packets [91], though still far from the lifetimes expected for nondispersive wave packets in one electron Rydberg systems [19,89]. Though, from the point of view of coherent control, it is precisely the long lifetime which makes these objects so interesting (they allow the "storage" of electronic density at essentially arbitrary locations of phase space), calling for further numerical or semiclassical studies in the future.

VI. SUMMARY AND CONCLUSIONS

We have given a detailed description of an *ab initio* treatment of planar helium under periodic driving. Our accurate numerical treatment provides, on the one hand, a complete description of the spectrum of unperturbed 2D helium, and, on the other hand, a description of the dynamics of the near-resonantly driven atom in the doubly excited spectral range.

The method developed in this paper can be adapted easily to account for the motion of the nucleus, which may become relevant for different mass ratios, e.g., in the case of excitonic trions of two electron systems in quantum dots. Furthermore, our Floquet approach is valid in the entire nonrelativistic parameter range of the field, and thus opens new perspectives for a unified understanding of various driving-induced fragmentation processes of the three-body Coulomb problem.

ACKNOWLEDGMENTS

It is a pleasure to thank Peter Schlagheck, Laurent Hilico, Benoît Grémaud, and Dominique Delande for lots of illuminating discussions and insight. Access to the computing facilities of the Rechenzentrum Garching der Max-Planck-Gesellschaft and of the Leibniz-Rechenzentrum der Bayerischen Akademie der Wissenschaft (under the Grand Challenge program), as well as partial financial support by the PROCOPE Program of DAAD is gratefully acknowledged.

APPENDIX: VISUALIZATION OF THE WAVE FUNCTIONS

Wave functions in the field-free case

The electronic density of a given state $|E\rangle$ can be obtained from the projection operator [82,92,93]

$$|E\rangle\langle E| = \frac{1}{2\pi i}\sum_i \left\{ \frac{R(-\theta)|E_{i\theta}\rangle\langle\overline{E_{i\theta}}|R(\theta)}{E_{i\theta}-E} - \frac{R(-\theta)|\overline{E_{i\theta}}\rangle\langle E_{i\theta}|R(\theta)}{\overline{E_{i\theta}}-E} \right\} \tag{A1}$$

on the given state, where $\langle\overline{E_{i\theta}}|$ denotes the complex conjugate of $\langle E_{i\theta}|$, i.e., the transpose of $\langle E_{i\theta}|$. The electronic probability density in configuration space reads [93]

$$\begin{aligned} |\Psi_E(\boldsymbol{r})|^2 &= \langle \boldsymbol{r}|E\rangle\langle E|\boldsymbol{r}\rangle \\ &= \frac{1}{\pi}\,\mathrm{Im}\sum_j \frac{\langle \boldsymbol{r}|R(-\theta)|E_{j\theta}\rangle\langle\overline{E_{j\theta}}|R(\theta)|\boldsymbol{r}\rangle}{E_{j\theta}-E} \\ &= \frac{1}{\pi}\,\mathrm{Im}\sum_j \frac{\langle \boldsymbol{r}|R(-\theta)|E_{j\theta}\rangle^2}{E_{j\theta}-E}. \end{aligned} \tag{A2}$$

A well-isolated resonance $|E_{j\theta}\rangle$ with $E_{j\theta} \simeq E$ and $|E_{j\theta}-E_{i\theta}| \gg |E_{j\theta}-E|, \forall i \neq j$, gives the dominant contribution to the above sum, and justifies the *single pole approximation* [93]

$$|\Psi_E(\boldsymbol{r})|^2 \simeq \frac{1}{\pi|\mathrm{Im}\,E_{j\theta}|}\,\mathrm{Re}\,\langle \boldsymbol{r}|R(-\theta)|E_{j\theta}\rangle^2. \tag{A3}$$

$\langle \boldsymbol{r}|R(-\theta)|E_{j\theta}\rangle$ in terms of the basis set (31) reads

$$\langle \boldsymbol{r}|R(-\theta)|E_{j\theta}\rangle = \sum_{\boldsymbol{n}} \langle \boldsymbol{r}|\boldsymbol{n}\rangle^{+\epsilon_x+\epsilon_y}\langle \boldsymbol{n}|R(-\theta)|E_{j\theta}\rangle, \tag{A4}$$

where $\boldsymbol{n}$ denotes the set of quantum numbers n_1, n_2, n_3, and n_4. Therefore, we need an expression for the basis states

$|n_1n_2n_3n_4\rangle^{+\epsilon_x}$ in the coordinate representation, together with a matrix representation of the operator $R(-\theta)$. In both cases, it is sufficient to derive that for the product states $|n_1n_2n_3n_4\rangle$, by virtue of Eqs. (30) and (31).

Since the circular operators given by Eq. (24) are independently defined for the pairs (x_p,y_p) and (x_m,y_m) of parabolic coordinates, $\langle \boldsymbol{r}|n_1n_2n_3n_4\rangle$, if written in parabolic coordinates, can be expressed as a product of two functions depending on (x_p,y_p) and (x_m,y_m), respectively, i.e., $\langle \boldsymbol{r}|n_1n_2n_3n_4\rangle=\langle x_p,y_p|n_1n_2\rangle\langle x_m,y_m|n_3n_4\rangle$, where

$$\langle x_p,y_p|n_1n_2\rangle = \sqrt{\frac{1}{\pi}}\sqrt{\frac{n_p!}{(n_p+|m_p|)!}}e^{im_p\phi_p} \times r_p^{|m_p|}e^{-r_p^2/2}L_{n_p}^{(|m_p|)}(r_p^2), \tag{A5}$$

with $n_p=\min\{n_1,n_2\}$, $m_p=n_1-n_2$, and $L_{n_p}^{(|m_p|)}(r)$ the generalized Laguerre polynomial [94]. By analogy, the expression for $\langle r_m,\phi_m|n_3n_4\rangle$ has precisely the same form.

For the calculation of the matrix elements of $R(-\theta)$, we note that this operator can be expressed as a product of two rotation operators $R_p(-\theta)$ and $R_m(-\theta)$, acting on the spaces (x_p,y_p) and (x_m,y_m), respectively, and thus, as before

$$\langle n_1n_2n_3n_4|R(-\theta)|n_1'n_2'n_3'n_4'\rangle = \langle n_1n_2|R_p(-\theta)|n_1'n_2'\rangle\langle n_3n_4|R_m(-\theta)|n_3'n_4'\rangle. \tag{A6}$$

The matrix elements of $R_p(-\theta)$ in the representation given by the product states $|n_1n_2\rangle$ read [65]

$$\langle n_1n_2|R_p(-\theta)|n_1'n_2'\rangle = (-1)^{n_p'}\sqrt{\binom{n_p+|m_p|}{n_p}\binom{n_p'+|m_p|}{n_p'}}i^{n_p+n_p'} \times(\sin\theta)^{n_p+n_p'}(\cos\theta)^{-(n_p+n_p'+|m_p|+1)} \times F\left(-n_p,-n_p',|m_p|+1;-\frac{1}{\sin^2\theta}\right)\delta_{m_pm_p'}, \tag{A7}$$

where $n_p=\min\{n_1,n_2\}$, $m_p=n_1-n_2$, $n_p'=\min\{n_1',n_2'\}$, $m_p'=n_1'-n_2'$, and $F(a,b,c;x)$ is the hypergeometric function [94] (which here reduces to a polynomial). Analogously, we obtain the expression for the matrix elements of $R_m(-\theta)$, with a formally identical result.

Combining Eqs. (A7), (A5), and (A3), we obtain the electronic density in configuration space.

Husimi distributions of frozen planet states

The Husimi function $W_\psi(q,p)$ of a quantum state $|\psi\rangle$ is defined as the diagonal element of the associated density matrix with respect to harmonic oscillator coherent states $|z\rangle$ with squeezing parameter ω_s (which is nothing but the harmonic oscillator frequency), i.e., $W_\psi(q,p)=|\langle z|\psi\rangle|^2$. The coherent state $|z\rangle$ is a minimum uncertainty Gaussian wave packet with coordinate representation

$$\langle r|z\rangle = \exp\left(-\frac{1}{2}\omega_s(r-q)^2-irp\right), \tag{A8}$$

centered at the point (p,q) in phase space [95] (with appropriate scaling according to $z=(\sqrt{\omega_s}q+ip/\sqrt{\omega_s})/\sqrt{2}$).

However, for the study of the FPC this definition has to be amended [20,73]. Let us assume that x_1 and p_1 (x_2 and p_2) are the position and the momentum of the outer (inner) electron in the collinear FPC. Then, for each point (x_1,p_1) of the Poincaré surface of section shown in Fig. 5(a): $x_2=0$ and $p_2=0$. Hence, in order to compare the 2D FPS with the classical phase space of the collinear FPC, we first have to project the 2D FPS onto the (x,p_x) subspace, and then to calculate its overlap with the Gaussian wave packets in (x_1,p_{x_1}) space, while imposing $x_2\simeq 0$. For this purpose, Eq. (A8) has to be multiplied by $\delta(y_1)\delta(x_2-x_2^0)\delta(y_2)$, where x_2^0 is close to zero (though not precisely zero, since the wave function vanishes at the origin). We finally obtain for the modified coherent state

$$\phi_{q,p}(x_1,y_1,x_2,y_2) = e^{-(1/2)\omega_s(x_1-q)^2-ix_1p}\delta(y_1)\delta(x_2-x_2^0)\delta(y_2), \tag{A9}$$

where we choose $\omega_s=\omega_I=0.3(N-1/2)^{-3}$, i.e., the intrinsic frequency (43) of the FPC, as squeezing parameter.

The projected Husimi function $W_\psi(q,p)=|\langle\phi_{q,p}|E\rangle|^2$ of an energy eigenstate $|E\rangle$, obtained after substitution of the projection operator (A1) in the single resonance approximation, is finally given by [20]

$$W_\psi(q,p)\simeq\frac{1}{\pi|\mathrm{Im}\,E_{j\theta}|}\,\mathrm{Re}\int d\boldsymbol{r}\phi_{q,p}(\boldsymbol{r})\langle\boldsymbol{r}|R(-\theta)|E_{j\theta}\rangle \times\int d\boldsymbol{r}'\phi_{q,p}^*(\boldsymbol{r}')\langle\boldsymbol{r}'|R(-\theta)|E_{j\theta}\rangle. \tag{A10}$$

Time evolution of the wave functions

The temporal dynamics of the electronic density at real energy $E=E_p$ is essentially given by the time evolution of a Floquet eigenstate $|E_{p\theta}\rangle$ under the action of the time evolution operator [66,82]

$$U(t_2,t_1)=\sum_{j,k_1,k_2}e^{-i\varepsilon_j(t_2-t_1)}e^{ik_1\omega t_1}e^{-ik_2\omega t_2} \times R(-\theta)|\phi_{\varepsilon_j,\theta}^{k_2}\rangle\overline{\langle\phi_{\varepsilon_j,\theta}^{k_1}|}R(\theta). \tag{A11}$$

If $|\phi_{p\theta}^k\rangle$ are the Fourier components of $|E_{p\theta}\rangle$ at $t=0$ (i.e., $|E_{p\theta}\rangle=\Sigma_k|\phi_{p\theta}^k\rangle$) and $\psi_p(\boldsymbol{r},t)=U(t,0)|E_p\rangle$, at any time t, we obtain

$$|\psi_p(\boldsymbol{r},t)|^2=e^{2(\mathrm{Im}\,\varepsilon_{p,\theta})t}\,\mathrm{Re}\sum_{k,k'}e^{-i(k-k')\omega t} \times\langle\boldsymbol{r}|R(-\theta)|\phi_{\varepsilon_j,\theta}^k\rangle\langle\boldsymbol{r}|R(-\theta)|\phi_{\varepsilon_j,\theta}^{k'}\rangle, \tag{A12}$$

as a generalization of Eq. (A3), up to normalization. Here,

the product $\langle \boldsymbol{r}|R(-\theta)|\phi^{k'}_{\varepsilon_j,\theta}\rangle$ is equivalent to the expression (A4), and can be calculated in precisely the same way as described in the previous section.

Husimi distributions of driven frozen planet states

For the driven case, using a similar reasoning as the one presented in Sec. 3 of this appendix for the deduction of the electronic density (A12) of Floquet states in configuration space, the time evolution operator (A11), together with Eq. (A9), yields the following expression for the projection of the Husimi function of a Floquet eigenstate $|E_p\rangle$ on the collinear subspace along the field polarization axis:

$$W_\psi(q,p,t) = \left| \int d\boldsymbol{r}\, \phi_{q,p}(\boldsymbol{r})\phi_p(\boldsymbol{r},t) \right|^2$$

$$= e^{2\,\mathrm{Im}(\varepsilon_{p,\theta}t)}\,\mathrm{Re}\sum_{k,k'} e^{-i(k-k')\omega t} \int d\boldsymbol{r}\,\phi^*_{q,p}(\boldsymbol{r})\langle \boldsymbol{r}|R(-\theta)$$

$$\times|\phi^k_{\varepsilon_p,\theta}\rangle \int d\boldsymbol{r}'\,\phi_{q,p}(\boldsymbol{r}')\langle \boldsymbol{r}'|R(-\theta)|\phi^{k'}_{\varepsilon_p,\theta}\rangle, \quad \text{(A13)}$$

with $\phi_{q,p}(\boldsymbol{r})$ the projection (A9) of the coherent states, and $|\phi^k_{\varepsilon_p,\theta}\rangle$ the Fourier components of the Floquet state $|\phi_{\varepsilon_p,\theta}(t)\rangle$.

[1] A. Einstein, Verh. Dtsch. Phys. Ges. **19**, 82 (1917).
[2] M. C. Gutzwiller, J. Math. Phys. **8**, 1979 (1967).
[3] M. C. Gutzwiller, J. Math. Phys. **12**, 343 (1971).
[4] G. S. Ezra, K. Richter, G. Tanner, and D. Wintgen, J. Phys. B **24**, L413 (1991).
[5] D. Wintgen, K. Richter, and G. Tanner, Chaos **2**, 19 (1992).
[6] G. Tanner, K. Richter, and J. M. Rost, Rev. Mod. Phys. **72**, 497 (2000).
[7] D. N. Fittinghoff, P. R. Bolton, B. Chang, and K. C. Kulander, Phys. Rev. Lett. **69**, 2642 (1992).
[8] B. Walker, B. Sheehy, L. F. DiMauro, P. Agostini, K. J. Schafer, and K. C. Kulander, Phys. Rev. Lett. **73**, 1227 (1994).
[9] K. J. Schafer, B. Yang, L. F. DiMauro, and K. C. Kulander, Phys. Rev. Lett. **70**, 1599 (1993).
[10] B. Yang, K. J. Schafer, B. Walker, K. C. Kulander, P. Agostini, and L. F. DiMauro, Phys. Rev. Lett. **71**, 3770 (1993).
[11] P. B. Corkum, Phys. Rev. Lett. **71**, 1994 (1993).
[12] A. Becker and F. H. M. Faisal, Phys. Rev. Lett. **84**, 3546 (2000).
[13] T. Weber, H. Giessen, M. Weckenbrock, G. Urbash, A. Staudte, L. Spielberger, O. Jagutzki, V. Mergel, M. Vollmer, and R. Dörner, Nature (London) **405**, 658 (2000).
[14] R. Moshammer, *et al.*, Phys. Rev. A **65**, 035401 (2002).
[15] V. L. B. de Jesus, B. Feuerstein, K. Zrost, D. Fischer, A. Rudenko, F. Afaneh, C. D. Schröter, R. Moshammer, and J. Ullrich, J. Phys. B **37**, L161 (2004).
[16] K. Richter and D. Wintgen, Phys. Rev. Lett. **65**, 1965 (1990).
[17] K. Richter, J. S. Briggs, D. Wintgen, and E. A. Solovev, J. Phys. B **25**, 3929 (1992).
[18] P. Schlagheck and A. Buchleitner, J. Phys. B **31**, L489 (1998).
[19] A. Buchleitner, D. Delande, and J. Zakrzewski, Phys. Rep. **368**, 409 (2002).
[20] P. Schlagheck and A. Buchleitner, Eur. Phys. J. D **22**, 401 (2003).
[21] P. Schlagheck and A. Buchleitner, Europhys. Lett. **46**, 24 (1999).
[22] W. Zhao, J. J. Mestayer, J. C. Lancaster, F. B. Dunning, C. O. Reinhold, S. Yoshida, and J. Burgdörfer, Phys. Rev. Lett. **97**, 253003 (2006).
[23] P. Schlagheck and A. Buchleitner, Physica D **131**, 110 (1999).
[24] J. Madroñero, P. Schlagheck, L. Hilico, B. Grémaud, D. Delande, and A. Buchleitner, Europhys. Lett. **70**, 183 (2005).
[25] M. Kalinski, L. Hansen, and D. Farrelly, Phys. Rev. Lett. **95**, 103001 (2005).
[26] A. Bürgers, D. Wintgen, and J. M. Rost, J. Phys. B **28**, 3163 (1995).
[27] B. Grémaud and P. Gaspard, J. Phys. B **31**, 1671 (1998).
[28] V. I. Korobov, Phys. Rev. A **61**, 064503 (2000).
[29] E. Foumouo, G. L. Kamta, G. Edah, and B. Piraux, Phys. Rev. A **74**, 063409 (2006).
[30] K. Taylor, J. Parker, K. Meharg, and D. Dundas, Eur. Phys. J. D **26**, 67 (2003).
[31] P. Lambropoulos, P. Maragakis, and J. Zhang, Phys. Rep. **203**, 305 (1998).
[32] A. Scrinzi and B. Piraux, Phys. Rev. A **58**, 1310 (1998).
[33] J. Purvis, M. Dörr, M. Terao-Dunseath, C. J. Joachain, P. G. Burke, and C. J. Noble, Phys. Rev. Lett. **71**, 3943 (1993).
[34] J. Madroñero, Ph.D. thesis, Ludwig-Maximilians-Universität München, 2004, http://edoc.ub.uni-muenchen.de/archive/00002187/
[35] K. Sacha and B. Eckhardt, Phys. Rev. A **63**, 043414 (2001).
[36] B. Stébé and A. Ainane, Superlattices Microstruct. **5**, 545 (1989).
[37] K. Kheng, R. T. Cox, Y. Merle d'Aubigné, F. Bassani, K. Saminadayar, and S. Tatarenko, Phys. Rev. Lett. **71**, 1752 (1993).
[38] G. Finkelstein, H. Shtrikman, and I. Bar-Joseph, Phys. Rev. Lett. **74**, 976 (1995).
[39] H. Buhmann, L. Mansouri, J. Wang, P. H. Beton, N. Mori, L. Eaves, M. Henini, and M. Potemski, Phys. Rev. B **51**, 7969 (1995).
[40] A. J. Shields, M. Pepper, D. A. Ritchie, M. Y. Simmons, and G. A. C. Jones, Phys. Rev. B **51**, 18049 (1995).
[41] N. Paganotto, J. Siviniant, D. Coquillat, D. Scalbert, J.-P. Lascaray, and A. V. Kavokin, Phys. Rev. B **58**, 4082 (1998).
[42] R. G. Nazmitdinov, N. S. Simonović, and J. M. Rost, Phys. Rev. B **65**, 155307 (2002).
[43] I. C. Percival, Proc. R. Soc. London, Ser. A **353**, 289 (1977).
[44] M. G. Floquet, Ann. Sci. Ec. Normale Super. **12**, 47 (1883).
[45] J. H. Shirley, Phys. Rev. **138**, B979 (1965).
[46] Y. B. Zeldovich, Sov. Phys. JETP **24**, 1006 (1967).
[47] A. Lichtenberg and M. A. Lieberman, *Regular and Chaotic Dynamics* (Springer-Verlag, New York, 1992).
[48] J. Aguilar and J. M. Combes, Commun. Math. Phys. **22**, 269

(1971).
[49] E. Balslev and J. M. Combes, Commun. Math. Phys. **22**, 280 (1971).
[50] Y. K. Ho, Phys. Rep. **99**, 1 (1983).
[51] S. Graffi, V. Grecchi, and H. J. Silverstone, Ann. I.H.P. Phys. Theor. **42**, 215 (1985).
[52] K. Yajima, Commun. Math. Phys. **87**, 331 (1982).
[53] M. Reed and B. Simon, *Methods of Modern Mathematical Physics IV. Analysis of Operators* (Academic Press, New York, 1978).
[54] L. Hilico, B. Grémaud, T. Jonckheere, N. Billy, and D. Delande, Phys. Rev. A **66**, 022101 (2002).
[55] M. Pont and R. Shakeshaft, Phys. Rev. A **43**, 3764 (1991).
[56] L. Landau and E. Lifchitz, *Quantum Mechanics* (Mir, Moscow, 1966).
[57] R. Loudon, *The Quantum Theory of Light* (Clarendon Press, Oxford, 1984).
[58] See EPAPS Document No. E-PLRAAN-77-068805 for the complete expressions of the representation in creation and annihilation operators, and for the complete set of selection rules and of the associated matrix elements. For more information on EPAPS, see http://www.aip.org/pubservs/epaps.html.
[59] C. Lanczos, J. Res. Natl. Bur. Stand. **45**, 225 (1950).
[60] B. N. Parlett and D. S. Scott, Math. Comput. **33**, 217 (1979).
[61] T. Ericsson and A. Ruhe, Math. Comput. **35**, 1251 (1980).
[62] A. Krug, Ph.D. thesis, Ludwig-Maximilians-Universität München, 2001, http://edoc.ub.uni-muenchen.de/archive/00000336/.
[63] http://www.mpi-forum.org/docs/docs.html
[64] M. Snir, S. Otto, S. Huss-Lederman, D. W. Walker, and J. J. Dongarra, *MPI: The Complete Reference* (MIT Press, Cambridge, 1995).
[65] D. Delande, Thèse d'état, Université Pierre et Marie Curie (Paris 6), 1988.
[66] A. Buchleitner, D. Delande, and J. Gay, J. Opt. Soc. Am. B **12**, 505 (1994).
[67] C. Cohen-Tannoudji, B. Diu, and F. Laloë, *Quantum Mechanics* (Wiley, Paris, 1977).
[68] J. von Neumann and E. P. Wigner, Phys. Z. **30**, 467 (1929).
[69] L. D. Landau, Phys. Z. Sowjetunion **2**, 46 (1932).
[70] C. Zener, Proc. R. Soc. London, Ser. A **137**, 696 (1932).
[71] H. Friedrich and D. Wintgen, Phys. Rev. A **32**, 3231 (1985).
[72] K. Richter, G. Tanner, and D. Wintgen, Phys. Rev. A **48**, 4182 (1993).
[73] P. Schlagheck, Ph.D. thesis, Technische Universität München, 1999.
[74] A. López-Castillo, M. A. M. de Aguiar, and A. M. O. de Almeida, J. Phys. B **29**, 197 (1996).
[75] V. N. Ostrovsky and N. V. Prudov, J. Phys. B **28**, 4435 (1995).
[76] K. Richter and D. Wintgen, J. Phys. B **24**, L565 (1991).
[77] U. Eichmann, V. Lange, and W. Sandner, Phys. Rev. Lett. **64**, 274 (1990).
[78] A. Assion, T. Baumert, M. Bergt, T. Brixner, B. Kiefer, V. Seyfried, M. Strehle, and G. Gerber, Science **282**, 919 (1998).
[79] T. C. Weinacht, J. Ahn, and P. H. Bucksbaum, Nature (London) **397**, 233 (1999).
[80] D. G. Arbó, C. O. Reinhold, and J. Burgdörfer, Phys. Rev. A **69**, 023409 (2004).
[81] L. G. Hanson and P. Lambropoulos, Phys. Rev. Lett. **74**, 5009 (1995).
[82] A. Buchleitner, Ph.D. thesis, Université Pierre et Marie Curie (Paris 6), 1993, URL: http://tel.ccsd.cnrs.fr/tel-00011885
[83] I. Białynicki-Birula, M. Kalinski, and J. H. Eberly, Phys. Rev. Lett. **73**, 1777 (1994).
[84] A. F. Brunello, T. Uzer, and D. Farrelly, Phys. Rev. Lett. **76**, 2874 (1996).
[85] D. Delande and A. Buchleitner, Adv. At., Mol., Opt. Phys. **34**, 85 (1994).
[86] F. B. Dunning, J. C. Lancaster, J. Burgdörfer, C. O. Reinhold, and S. Yoshida, Adv. At., Mol., Opt. Phys. **52**, 49 (2005).
[87] H. Maeda and T. F. Gallagher, Phys. Rev. Lett. **92**, 133004 (2004).
[88] H. Maeda, D. V. L. Norum, and T. F. Gallagher, Science **307**, 1757 (2005).
[89] H. Maeda and T. F. Gallagher, Phys. Rev. A **75**, 033410 (2007).
[90] S. N. Pisharody and R. R. Jones, Science **303**, 813 (2004).
[91] C. Raman, T. C. Weinacht, and P. H. Bucksbaum, Phys. Rev. A **55**, R3995 (1997).
[92] B. Grémaud, Ph.D. thesis, Université Pierre et Marie Curie (Paris 6), 1997, http://tel.ccsd.cnrs.fr/tel-00011786
[93] A. Buchleitner, B. Grémaud, and D. Delande, J. Phys. B **27**, 2663 (1994).
[94] M. Abramowitz and I. Stegun, *Handbook of Mathematical Functions* (Dover Publications, New York, 1972).
[95] L. Mandel and E. Wolf, *Optical Coherence and Quantum Optics* (Cambridge University Press, New York, 1995).
[96] $\mathbb{T}_\omega = \mathbb{R}/2\pi\omega$, i.e., the unit circle.
[97] http://www.lrz-muenchen.de/services/compute/hlrb
[98] http://www.rzg.mpg.de/computing/IBM_P/